Gaussian-SLAM: Photo-realistic Dense SLAM with Gaussian Splatting

Vladimir Yugay   Yue Li   Theo Gevers   Martin R. Oswald

University of Amsterdam, Netherlands

{vladimir.yugay, y.li6, th.gevers, m.r.oswald}@uva.nl

vladimiryugay.github.io/gaussian_slam

ESLAM [34]	Point-SLAM [51]	Gaussian-SLAM (Ours)

Figure 1. **Rendering Results of Gaussian-SLAM in Comparison.** Embedded into a dense SLAM pipeline, the Gaussian splatting-based scene representation allows for very fast, photo-realistic rendering of scene views. This leads to unprecedented rendering quality, especially on real-world data like this TUM-RGBD [59] frame that contains many high-frequency details that other methods struggle to capture.

c

Abstract

We present a new dense simultaneous localization and mapping (SLAM) method that uses Gaussian splats as a scene representation. The new representation enables interactive-time reconstruction and photo-realistic rendering of real-world and synthetic scenes. We propose novel strategies for seeding and optimizing Gaussian splats to extend their use from multiview offline scenarios to sequential monocular RGBD input data setups. In addition, we extend Gaussian splats to encode geometry and experiment with tracking against this scene representation. Our method achieves state-of-the-art rendering quality on both real-world and synthetic datasets while being competitive in reconstruction performance and runtime.

1. Introduction

Simultaneous localization and mapping (SLAM) have been an active research topic for the past two decades [16, 23]. A major byproduct of that journey has been the investi- gation of various scene representations to either push the tracking performance and mapping capabilities or to adapt it for more complex downstream tasks like path planning or semantic understanding. Specifically, earlier works fo- cus on tracking using various scene representations like feature point clouds [15, 26, 40], surfels [53, 71], depth maps [43, 58], or implicit representations [14, 42, 44]. Later works focused more on the map quality and density. With the advent of powerful neural scene representations like neural radiance fields [38] that allow for high fidelity view- synthesis, a rapidly growing body of dense neural SLAM methods [19, 34, 51, 60, 62, 64, 81, 84] has been devel- oped. Despite their impressive gains in scene representation quality, these methods are still limited to small synthetic scenes and their re-rendering results are still far from being photo-realistic.

Recently, a novel scene representation based on Gaussian splatting [25] has been shown to deliver on-par or even better rendering performance than NeRFs while being an order of magnitude faster in rendering and optimization. Besides be- ing faster, this scene representation is directly interpretable and allows for direct scene editing which is a desirable prop-

erty for many downstream tasks. With these advantages, the Gaussian splatting representation lends itself to be applied in an online SLAM system with real-time demands and as such opens the door towards photo-realistic dense SLAM.

In this paper, we introduce Gaussian-SLAM, a dense RGBD SLAM system using Gaussian splats as scene representation which allows for almost photo-realistic re-rendering at interactive runtimes. An example of the high fidelity rendering output of Gaussian-SLAM is depicted in Fig. 1. This paper further reveals and discusses a variety of limitations of Gaussian splatting for SLAM and proposes solutions on how to tackle them. In summary, our **contributions** include:

- A dense RGBD SLAM approach that uses Gaussian splats as a scene representation allowing SOTA rendering results on real-world scenes in combination with substantially faster rendering.
- An extension of Gaussian splatting to better encode geometry allowing reconstruction beyond radiance fields in monocular setup.
- As the adaptation of the original Gaussian splatting from an offline to an online approach is by no means straightforward, we propose an online learning method for Gaussian splats that splits the map into sub-maps and introduces efficient seeding and optimization strategies.
- We further investigate frame-to-model tracking with Gaussian splatting via photometric error minimization and compare it to off-the-shelf frame-to-frame tracking.

All source code and data will be made publicly available.

2. Related Work

Dense Visual SLAM and Online Mapping. The seminal work of Curless and Levoy [12] set the stage for a variety of 3D reconstruction methods using truncated signed distance functions (TSDF). A line of works was built upon it improving speed [42] through efficient implementation and volume integration, scalability through voxel hashing [21, 44, 46] and octree data structure [55], and tracking with sparse image features [5] and loop closure [6, 14, 43, 53]. Tackling the problem of unreliable depth maps, RoutedFusion [68] introduced a learning-based fusion network for updating the TSDF in volumetric grids. This concept was further evolved by NeuralFusion [69] and DI-Fusion [19], which adopt implicit learning for scene representation, enhancing their robustness against outliers. Recent research has successfully achieved dense online reconstruction using solely RGB cameras [4, 9, 27, 41, 52, 56, 61] bypassing the need for depth data.

Recently, test-time optimization methods have become popular due to their ability to adapt to unseen scenes on the fly. Continuous Neural Mapping [74], for instance, employs a continual mapping strategy from a series of depth maps

to learn scene representation. Inspired by Neural Radiance Fields [38], there has been huge progress in dense surface reconstruction [45, 65] and accurate pose estimation [3, 29, 50, 67]. These efforts have led to the development of comprehensive dense SLAM systems [34, 60, 75, 81, 84, 85], showing a trend in the pursuit of precise and reliable visual SLAM. A comprehensive survey on online RGBD reconstruction can be found in [86].

While the latest neural methods show impressive rendering capabilities on synthetic data, they struggle when applied to real-world data. Further, these methods are not yet practical for real-world applications due to computation requirements, slow speed, and the challenges in incorporating pose updates, as the neural representations rely on positional encoding. In contrast, our method shows impressive performance on real-world data, has a competitive runtime, and uses a scene representation that naturally allows pose updates.

Scene Representations for SLAM. The majority of dense SLAM 3D scene representations are either grid-based, point-based, network-based, or hybrid. Among these, grid-based techniques are perhaps the most extensively researched. They further divide into methods using dense grids [4, 10, 12, 28, 42, 61, 68–71, 82–84], hierarchical octrees [7, 30, 31, 35, 55, 75] and voxel hashing [14, 21, 39, 44, 65] for efficient memory management. Grids offer the advantage of simple and quick neighborhood lookups and context integration. However, a key limitation is the need to predefine grid resolution, which is not easily adjustable during reconstruction. This can result in inefficient memory usage in empty areas while failing to capture finer details due to resolution constraints.

Point-based approaches address some of the grid-related challenges and have been effectively utilized in 3D reconstruction [6, 8, 11, 22, 24, 53, 71, 79]. Unlike grid resolution, the density of points in these methods does not have to be predetermined and can naturally vary throughout the scene. Moreover, point sets can be efficiently concentrated around surfaces, not spending memory on modeling empty space. The trade-off for this adaptability is the complexity of finding neighboring points, as point sets lack structured connectivity. In dense SLAM, this challenge can be mitigated by transforming the 3D neighborhood search into a 2D problem via projection onto keyframes [53, 71], or by organizing points within a grid structure for expedited searching [73].

Network-based methods for dense 3D reconstruction provide a continuous scene representation by implicitly modeling it with coordinate-based networks [1, 27, 36, 47, 60, 64, 65, 74, 76, 81]. This representation can capture high-quality maps and textures. However, they are generally unsuitable for online scene reconstruction due to their inability to update local scene regions and to scale for larger scenes. More recently, a hybrid representation combining the advantages of point-based and neural-based was proposed [51]. While

addressing some of the issues of both representations it struggles with real-world scenes, and cannot seamlessly integrate trajectory updates in the scene representation.

Outside these three primary categories, some studies have explored alternative representations like surfels [17, 37] and neural planes [34, 49]. Parameterized surface elements are generally not great at modeling a flexible shape template while feature planes struggle with scene reconstructions containing multiple surfaces, due to their overly compressed representation. Recently, Kerbl *et al.* [25] proposed to represent a scene with 3D Gaussians. The scene representation is optimized via differential rendering with multi-view supervision. While being very efficient and achieving impressive rendering results, this representation is tailored for fully-observed multi-view environments and does not encode geometry well. Concurrent with our work, [72, 77, 78] focus on dynamic scene reconstruction, and [33] on tracking. However, they are all offline methods and are not suited for monocular dense SLAM setups.

Unlike others, we use 3D Gaussians in an online scenario with a monocular RGBD input stream. Moreover, we extend 3D Gaussians to encode accurate geometry while being optimized in a single-view setup for a small number of iterations.

3. Gaussian Splatting and its Limitations

In this section we revisit the original offline Gaussian Splatting [25] approach, while following the mathematical formulation of [33]. Additionally, we provide an analysis of Gaussian splatting properties that make it challenging to apply the original implementation directly in a SLAM setting. We pinpoint and discuss specific cases where this method fails or proves ineffective, thereby identifying the potential need for modifications or alternative approaches in the context of SLAM applications.

Gaussian Splatting [25] is an effective method for representing 3D scenes with novel-view synthesis capability. This approach is notable for its speed, without compromising on the rendering quality. Originally, 3D Gaussians are initialized from a sparse SfM point cloud of a scene. Having a set of images observing the scene from different angles, the Gaussian parameters are optimized using differentiable rendering while 3D Gaussians are adaptively added or removed to the representation based on a set of heuristics.

The influence of a single 3D Gaussian on a physical point $p \in \mathbb{R}^3$ in 3D space is evaluated with the function:

$$f^{3D}(p) = \text{sigmoid}(o) \exp\left(-\frac{1}{2}(p-\mu)^T \Sigma^{-1}(p-\mu)\right),$$
(1)

where $\mu \in \mathbb{R}^3$ is a 3D Gaussian mean, $\Sigma = RSS^T R^T \in \mathbb{R}^{3,3}$ is the covariance matrix computed with $S \in \mathbb{R}^3$ scaling

and $R \in \mathbb{R}^{3,3}$ components, and $o \in \mathbb{R}$ is opacity. The 3D Gaussians are projected to the image plane using the equations [87]:

$$\mu^{2D} = K\big((E\mu)/(E\mu)_z\big) \ , \tag{2}$$
$$\Sigma^{2D} = JE\Sigma E^T J^T \ , \tag{3}$$

where K is the intrinsic matrix, E is the extrinsic matrix in camera-to-world coordinates, and J is the Jacobian of the point projection in Eq. (2), *i.e.* $\frac{\partial \mu^{2D}}{\partial \mu}$. The pixel color is influenced by all Gaussians which intersect with the ray cast from that specific pixel. The color is computed as a weighted average of the projected 3D Gaussians:

$$C_{\text{pix}} = \sum_{i \in V} c_i f_{i,\text{pix}}^{2D} \prod_{j=1}^{i-1}(1 - f_{j,\text{pix}}^{2D}) \ , \tag{4}$$

where V is the set of the Gaussians influencing the pixel, $f_{i,\text{pix}}^{2D}$ is the equivalent of the formula for f^{3D} except with the 3D means and covariance matrices replaced with the 2D splatted versions, and c_i is an RGB color of each Gaussian. Every term along the ray cast for a pixel is down-weighted by the transmittance term which accounts for the influence of the previously encountered Gaussians.

Limitations of Gaussian Splatting for SLAM. Due to its speed advantages, 3D Gaussian splatting [25] seems a great match for the requirements of a dense SLAM system. However, being designed for multi-camera environments with good coverage of observations, its application to monocular SLAM presents multiple unique challenges.

▷ **Seeding strategy for online SLAM:** As stated above, the original seeding strategy builds upon a sparse point cloud of surface points and adaptively creates and removes Gaussians during the optimization. Such iterative dynamic behavior potentially leads to large variations in mapping iterations and compute time which is rather undesirable for SLAM.

▷ **Online optimization:** A vanilla online implementation might just optimize over all frames, but for longer sequences, this becomes too slow for interactive frame rates.

▷ **Catastrophic forgetting in online optimization:** To avoid the linear growth in per-frame mapping with every new frame, an alternative is to optimize the Gaussian scene representation only with the current frame. While the optimization will quickly converge to fit the new training frame very well, previously mapped views will be severely degraded. This applies to the Gaussian shapes, encompassing both scale and orientation, as well as to the spherical harmonic color encoding, where local function adjustments can significantly alter function values in other areas of the spherical domain, as illustrated by the cyan colors in Figs. 2a, 2e.

▷ **Highly randomized solutions:** For both offline and online cases, the result of a splatting optimization highly depends
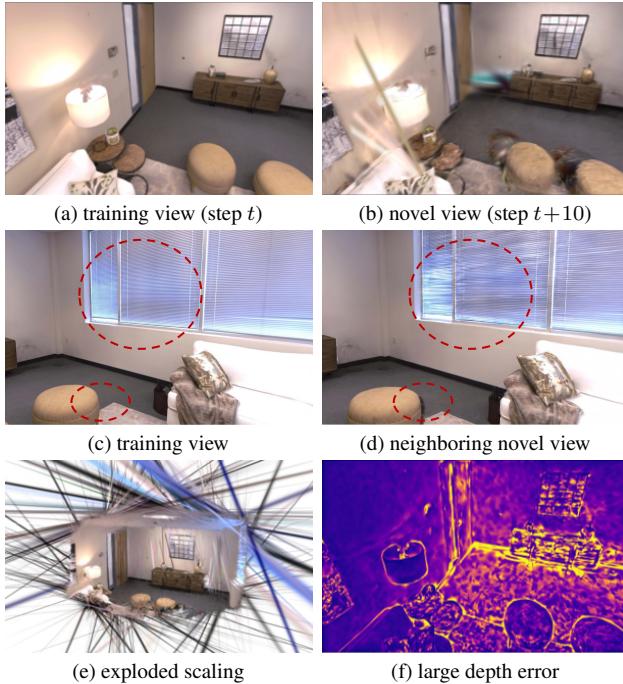
(a) training view (step t)

(b) novel view (step $t+10$)

(c) training view

(d) neighboring novel view

(e) exploded scaling

(f) large depth error

Figure 2. **Naive usage of Gaussian splatting for SLAM.** Fig. 2a and Fig. 2b show renderings of the naive SLAM pipeline for a training view and a novel view with a pose from 10 steps ahead. Fig. 2c and Fig. 2d show training and novel views from directly neighboring frames for which color artifacts occur. Fig. 2e shows uncontrolled growth of 3D Gaussian parameters. Fig. 2f depicts larger depth errors after optimizing 3D Gaussians to a single frame seed at GT depth.

on the initialization of Gaussians. Also during the optimization, Gaussians may grow suddenly in different directions depending on the neighboring Gaussians. Finally, the inherent symmetries of the 3D Gaussians allow parameter alterations without affecting the loss function, resulting in non-unique solutions, a generally undesirable characteristic in optimization.

▷ **Poor extrapolation capabilities:** Related to the previous issue, Gaussians often grow uncontrollably into unobserved areas. While good view coverage in an offline setting constrains most Gaussians well, novel views in a sparse-view SLAM setting often contain artifacts resulting from previously under-constrained Gaussians. This is shown in Fig. 2a-2d and is especially harmful for model-based tracking.

▷ **Limited geometric accuracy:** Gaussian splatting is not adept at encoding precise geometry when used in a monocular setup. While geometry estimation is relatively good in a well-constrained setup with multiple views, the resulting depth maps from a single-camera setup are ineffective for 3D reconstruction, as shown in Fig. 2f.

4. Method

The key idea of our approach is to use 3D Gaussian scene representation [25] to enhance dense monocular SLAM. We extend traditional Gaussian splatting representation to encode not only the radiance fields but also detailed geometry. Furthermore, we tailor the mapping process to yield state-of-the-art rendering in a sequential monocular setup, a very challenging scenario for 3D Gaussian Splatting. Finally, we experiment with frame-to-model tracking utilizing 3D Gaussian scene representation. Fig. 3 provides an overview of our method. We now explain our pipeline, starting with map construction and optimization, followed by geometry encoding, and tracking.

4.1. 3D Gaussian-based Map

To preserve novel view synthesis, avoid catastrophic forgetting, and make the Gaussian mapping computationally feasible, we split the input sequence into sub-maps. Every sub-map consists of several keyframes and is represented with a separate 3D Gaussian point cloud. Formally, we define a sub-map Gaussian point cloud P^s as a collection of N 3D Gaussians

$$P^s = \{G(\mu_i^s, S_i^s, R_i^s, o_i^s, \mathrm{SH}_i^s) \,|\, i = 1, \ldots, N\} \;, \quad (5)$$

each with a mean $\mu_i^s \in \mathbb{R}^3$, scale $S_i^s \in \mathbb{R}^3$, rotation $R_i^s \in \mathbb{R}^4$, opacity $o_i^s \in \mathbb{R}$, and spherical harmonics parameters $\mathrm{SH}_i^s \in \mathbb{R}^{48}$. At any period of time, we grow and optimize only one active sub-map. We start a new sub-map after a fixed amount of keyframes. Every new keyframe adds additional 3D Gaussians to the active sub-map to account for the newly observed parts of the scene.

Building Sub-maps Progressively. Seeding the new Gaussians is a crucial step in building sub-maps. At every keyframe, we compute a dense point cloud from the input RGBD frame and pose estimated by the tracker. We sample M_u uniformly and M_c points in high color gradient regions from the input point cloud. For each sampled point we seed two Gaussians: one on the surface at the measured depth and one slightly behind the surface in the viewing direction. This anchoring strategy is similar to [51], with the difference that we do not seed additional Gaussians in front of the surface points. Selected points serve as the initial mean locations for new Gaussians. The new Gaussians are anisotropic since their scale is defined based on the proximity of the neighboring Gaussians within the active sub-map similar to [25].

Sub-map Optimization. We optimize the active sub-map every time new Gaussians are added to it. When a new sub-map is created we optimize it for a fixed number of iterations I_s w.r.t. to depth and color. During optimization, we freeze the means of the Gaussians to not distort the geometry obtained from the depth sensor. We do not clone or prune the
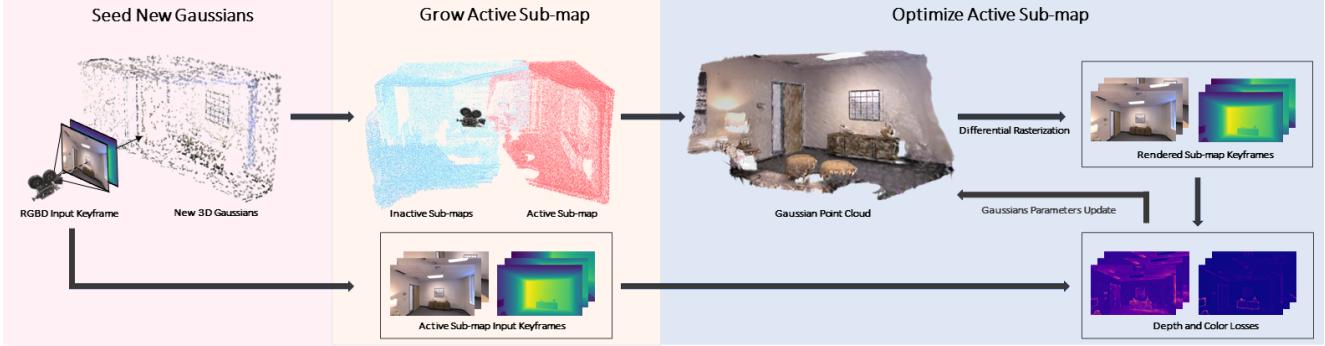
Figure 3. **Gaussian-SLAM Architecture.** Given an estimated camera pose, mapping is performed as follows. An input point cloud is subsampled and the locations for the new 3D Gaussians in the *active* sub-map are estimated based on the density of the sub-map. After the sparse set of new 3D Gaussians is added to the *active* sub-map Gaussian point cloud, they are jointly optimized. Depth maps and color images of all the keyframes that contributed to the active sub-map are rendered using a differential rasterizer. The 3D Gaussians' parameters are optimized by imposing depth, color re-rendering, and regularization losses against the input RGBD frame.

Gaussians as done in [25] to preserve geometry obtained from the depth sensor and to speed up optimization.

To counteract catastrophic forgetting, we optimize the active sub-map to be able to render the depth and color of all the keyframes seen in a given sub-map. In the original work [25] the scene representation is optimized for many iterations, and in every iteration, a new view is sampled randomly. However, this approach does not suit the SLAM setup where the amount of iterations is limited. Following the naive strategy leads to insufficient optimization of the new views in the sub-map or excessive time spent on optimization. We achieve the best results by iterating over all the keyframes in the active sub-map, but spending at least 50% of the iterations on the current keyframe.

4.2. Encoding Geometry and Color

3D Gaussians provide a natural way to render the color [25]. After the 3D Gaussians are splatted to the image plane, the color loss between the input color image and the rendered image is computed and optimized w.r.t. the Gaussian parameters. For the color supervision, we use a weighted combination of L_1 and SSIM [66] losses:

$$L_{\text{color}} = (1 - \lambda) \cdot |\hat{I} - I|_1 + \lambda\big(1 - \text{SSIM}(\hat{I}, I)\big) \ , \quad (6)$$

where I is the original image, $\hat{I}$ is the rendered image, and $\lambda = 0.2$. We estimate the depth at every pixel similar to color rendering as the sum of z coordinates of the Gaussians affecting this pixel weighted by the transmittance factor:

$$D_{\text{pix}} = \sum_{i \in S} z_i f_{i,\text{pix}}^{\text{2D}} \prod_{j}^{i-1} \big(1 - f_{j,\text{pix}}^{\text{2D}}\big) \ , \quad (7)$$

where z_i is the Z coordinate of the Gaussian mean μ_i in camera coordinate system. The loss is optimized with respect to the Gaussian parameters supervised by an input depth map.

The gradients with respect to the depth are derived similarly as for color. However, unlike color optimization, we do not update the means of the Gaussians during depth optimization to preserve the geometry obtained from the depth sensors. We use L_1 loss for depth optimization:

$$L_{\text{depth}} = |\hat{D} - D|_1 \ , \quad (8)$$

where $D, \hat{D} \in \mathbb{R}_{\geq 0}$ are the ground-truth and reconstructed depth maps, respectively. To prevent 3D Gaussians from scale explosion, we add a regularization loss L_{reg}. It is an L_2 loss applied to the scales of all the 3D Gaussians whose scale is larger than a threshold $\gamma = 10$. Finally, we optimize both color, depth, and regularization terms together:

$$L = L_{\text{color}} + \alpha \cdot L_{\text{depth}} + \beta \cdot L_{\text{reg}}, \quad (9)$$

with α and β both set to 1.

For color and depth rendering we cannot sample separate pixels since the effect of a single splatted Gaussian has a non-local influence on the rendered image. Therefore, for depth supervision, we fill in the missing values in the depth map with Navier-Stokes inpainting [2]. We implement depth rendering and gradient computation in CUDA which makes it efficient enough for SLAM applications.

4.3. Tracking

During tracking, the pose is initialized with multi-scale RGBD odometry [48]. Estimated relative transformations $\{\Delta\mathbf{R}', \Delta\mathbf{t}'\}$ are applied globally to the Gaussian positions and orientations of the active sub-map, and the image is rendered from the last estimated pose. The transformation from the last frame to the current frame is then obtained by inverting the relative transformation applied to the Gaussians:

$$\Delta R = (\Delta R')^{-1} \quad (10)$$
$$\Delta t = -(\Delta R) \times \Delta t'. \quad (11)$$

5

Method	Metric	0000	0059	0106	0169	0181	0207	Avg.
NICE-SLAM [84]	PSNR↑	18.71	16.55	17.29	18.75	15.56	18.38	17.54
	SSIM↑	0.641	0.605	0.646	0.629	0.562	0.646	0.621
	LPIPS↓	0.561	0.534	0.510	0.534	0.602	0.552	0.548
Vox-Fusion* [75]	PSNR↑	19.06	16.38	18.46	18.69	16.75	19.66	18.17
	SSIM↑	0.662	0.615	0.753	0.650	0.666	0.696	0.673
	LPIPS↓	0.515	0.528	0.439	0.513	0.532	0.500	0.504
ESLAM [34]	PSNR↑	15.70	14.48	15.44	14.56	14.22	17.32	15.29
	SSIM↑	0.687	0.632	0.628	0.656	0.696	0.653	0.658
	LPIPS↓	0.449	0.450	0.529	0.486	0.482	0.534	0.488
Point-SLAM [51]	PSNR↑	21.30	19.48	16.80	18.53	22.27	20.56	19.82
	SSIM↑	0.806	0.765	0.676	0.686	0.823	0.750	0.751
	LPIPS↓	0.485	0.499	0.544	0.542	0.471	0.544	0.514
Gaussian-SLAM (ours)	PSNR↑	**37.94**	**36.87**	**35.95**	**36.86**	**38.22**	**38.85**	**37.45**
	SSIM↑	**0.984**	**0.988**	**0.986**	**0.981**	**0.983**	**0.982**	**0.984**
	LPIPS↓	**0.066**	**0.058**	**0.067**	**0.072**	**0.074**	**0.071**	**0.068**

Table 1. **Rendering Performance on ScanNet [13].** We outperform existing dense neural RGBD methods on the commonly reported rendering metrics. For NICE-SLAM [84] and Vox-Fusion [75] we take the numbers from [85]. For qualitative results, see Fig. 4.

Method	Metric	fr1/ desk	fr1/ desk2	fr1/ room	fr2/ xyz	fr3/ office	Avg.
NICE-SLAM [84]	PSNR↑	13.83	12.00	11.39	17.87	12.890	13.59
	SSIM↑	0.569	0.514	0.373	0.718	0.554	0.545
	LPIPS↓	0.482	0.520	0.629	0.344	0.498	0.494
Vox-Fusion* [75]	PSNR↑	15.79	14.12	14.20	16.32	17.27	15.54
	SSIM↑	0.647	0.568	0.566	0.706	0.677	0.632
	LPIPS↓	0.523	0.541	0.559	0.433	0.456	0.502
ESLAM [34]	PSNR↑	11.29	12.30	9.06	17.46	17.02	13.42
	SSIM↑	0.666	0.634	0.929	0.310	0.457	0.599
	LPIPS↓	0.358	0.421	0.192	0.698	0.652	0.464
Point-SLAM [51]	PSNR↑	13.87	14.12	14.16	17.56	18.43	15.63
	SSIM↑	0.627	0.592	0.645	0.708	0.754	0.665
	LPIPS↓	0.544	0.568	0.546	0.585	0.448	0.538
Gaussian-SLAM (ours)	PSNR↑	**31.18**	**31.81**	**25.99**	**26.37**	**33.08**	**29.69**
	SSIM↑	**0.980**	**0.981**	**0.968**	**0.946**	**0.984**	**0.971**
	LPIPS↓	**0.067**	**0.068**	**0.125**	**0.148**	**0.060**	**0.093**

Table 2. **Rendering Performance on TUM-RGBD [58].** We outperform existing dense neural RGBD methods on the commonly reported rendering metrics by a huge margin. For NICE-SLAM [84] and Vox-Fusion [75] we take the numbers from [85]. For qualitative results, see Fig. 4.

Method	Metric	Rm0	Rm1	Rm2	Off0	Off1	Off2	Off3	Off4	Avg.
NICE-SLAM [84]	PSNR↑	22.12	22.47	24.52	29.07	30.34	19.66	22.23	24.94	24.42
	SSIM ↑	0.689	0.757	0.814	0.874	0.886	0.797	0.801	0.856	0.809
	LPIPS ↓	0.330	0.271	0.208	0.229	0.181	0.235	0.209	0.198	0.233
Vox-Fusion* [75]	PSNR↑	22.39	22.36	23.92	27.79	29.83	20.33	23.47	25.21	24.41
	SSIM↑	0.683	0.751	0.798	0.857	0.876	0.794	0.803	0.847	0.801
	LPIPS↓	0.303	0.269	0.234	0.241	0.184	0.243	0.213	0.199	0.236
ESLAM [34]	PSNR↑	25.25	25.31	28.09	30.33	27.04	27.99	29.27	29.15	27.80
	SSIM↑	0.874	0.245	0.935	0.934	0.910	0.942	0.953	0.948	0.921
	LPIPS↓	0.315	0.296	0.245	0.213	0.254	0.238	0.186	0.210	0.245
Point-SLAM [51]	PSNR↑	32.40	34.08	35.50	38.26	39.16	33.99	33.48	33.49	35.17
	SSIM↑	0.974	0.977	0.982	0.983	0.986	0.960	0.960	0.979	0.975
	LPIPS↓	0.113	0.116	0.111	0.100	0.118	0.156	0.132	0.142	0.124
Gaussian-SLAM (ours)	PSNR↑	**34.31**	**37.28**	**38.18**	**43.97**	**43.56**	**37.39**	**36.48**	**40.19**	**38.90**
	SSIM↑	**0.988**	**0.992**	**0.993**	**0.996**	**0.995**	**0.992**	**0.992**	**0.999**	**0.993**
	LPIPS↓	**0.082**	**0.068**	**0.074**	**0.045**	**0.066**	**0.078**	**0.079**	**0.066**	**0.069**

Table 3. **Rendering Performance on Replica [57].** We outperform all existing dense neural RGBD methods on the commonly reported rendering metrics. The numbers for NICE-SLAM [84] and Vox-Fusion [75] are taken from [85].

The re-rendered color loss is optimized with respect to the relative transformation.

Our experiments show that 3D Gaussians exhibit limited extrapolation capabilities, as evidenced by rendering artifacts when deviating from the initial trajectory and difficulties in reconstructing accurate depth maps at geometry discontinuities and within unseen regions. Optimizing the re-rendering loss for pose refinement shows worse tracking performance compared to other neural SLAM methods that use a similar approach but use implicit representation as shown in Tab. 5.

To assess the impact of these limitations, we carry out oracle experiments, where Gaussian sub-maps are firstly mapped using ground truth poses and then used by tracking. The oracle method achieves better accuracy than all other dense neural SLAM methods including DROID-SLAM [63]. This supports our claim that the tracking accuracy is limited by the extrapolation capability of the 3D Gaussian splats.

As frame-to-model tracking is currently unsatisfactory, we utilize the trajectories of DROID-SLAM [63] in obtaining all the results on rendering and reconstruction. We believe that enhancements in depth map rendering will further improve frame-to-model tracking accuracy in our method as evidenced by the oracle experiment.

5. Experiments

We first describe our experimental setup and then evaluate our method against state-of-the-art dense neural RGBD SLAM methods on Replica [57] as well as the real-world TUM-RGBD [59] and ScanNet [13] datasets. Further experiments and details are provided in the appendix.

Implementation Details. We set $M_u = 15000$ and $M_c = 20000$ for Replica, $M_u = 10000, M_c = 15000$ for TUM-RGBD, and $M_u = 55000, M_c = 20000$ for ScanNet. The number of iterations for the first frame in a sub-map is set to 1000 for all the datasets. The number of iterations for all the other frames in a sub-map is set to 500 for Replica and TUM-RGBD, and 1000 for ScanNet. Every 5th frame is considered as a keyframe for all the datasets. We use FAISS [20] GPU implementation for finding nearest neighbors when deciding which points to add as new Gaussians. We use Gaussian addition radius $\rho = 0.03m$ for Replica and TUM-RGBD, and $\rho = 0.07m$ for ScanNet. For all the datasets we spend at least 50% of iterations on the newly incoming keyframe. To mesh the scene, we render depth and color every fifth frame over the estimated trajectory and use TSDF Fusion [12] with voxel size 1 cm similar to [51]. Please refer to the appendix for more details.

Datasets. The Replica dataset [57] comprises high-quality 3D reconstructions of a variety of indoor scenes. We utilize

the publicly available dataset collected by Sucar *et al.* [60], which provides trajectories from an RGBD sensor. Further, we demonstrate that our framework can handle real-world data by using the TUM-RGBD dataset [59], as well as the ScanNet dataset [13]. The poses for TUM-RGBD were captured using an external motion capture system while ScanNet uses poses from BundleFusion [14].

Evaluation Metrics. The meshes, produced by marching cubes [32], are evaluated using the F-score being the harmonic mean of the Precision (P) and Recall (R). We use a distance threshold of 1 cm for all evaluations. We further provide the depth L1 metric for unseen views as in [84]. For tracking accuracy, we use ATE RMSE [59] and for rendering we provide the peak signal-to-noise ratio (PSNR), SSIM [66] and LPIPS [80]. Our rendering metrics are evaluated by rendering the full-resolution image along the estimated trajectory by the mapping interval similar to [51].

Baseline Methods. We primarily compare our method to existing state-of-the-art dense neural RGBD SLAM methods such as NICE-SLAM [84], Vox-Fusion [75], ESLAM [34] and Point-SLAM [51]. We reproduce the results from [75] using the open source code and report the results as Vox-Fusion*. For NICE-SLAM, we mesh the scene at resolution $1cm$ for a fair comparison. We could not obtain the rendering from GO-SLAM [81] for the evaluation since rendering function was not available at the time of submission.

5.1. Rendering Performance

Tab. 1 and Tab. 2 show our state-of-the art rendering performance on real-world datasets. Tab. 3 compares rendering performance and shows improvements over all the existing dense neural RGBD SLAM methods on synthetic data. Fig. 4 shows exemplary full-resolution renderings where Gaussian-SLAM yields more accurate details.

5.2. Reconstruction Performance

In Tab. 4 we compare our method to NICE-SLAM [84], Vox-Fusion [75], ESLAM [34], GO-SLAM [81] and Point-SLAM [51] in terms of the geometric reconstruction accuracy on the Replica dataset [57]. Our method performs on par with other existing dense SLAM methods.

5.3. Tracking Performance

Tab. 5 presents our tracking results together with oracle performance on the Replica dataset [57], comparing against other SOTA dense neural RGBD SLAM methods and DROID-SLAM [63]. Poses are first estimated with RGBD odometry implemented in Open3D based on [48, 54]. As discussed in Sec. 4.3, our tracking falls behind in accuracy while the oracle method consistently outperforms all other dense neural RGBD SLAM methods and also surpasses DROID-SLAM [63]. For all experiments, the depth loss is

not used due to the negative impact of the inaccurate depth map. More tracking results are provided in the appendix D.

5.4. Further Statistical Evaluation

Runtime Analysis. We report runtime usage on the Replica `office0` scene in Tab. 6. The mapping time is reported per iteration and per frame averaged over the full trajectory. **Limitations.** Although we have adapted Gaussian splatting for online dense SLAM, tracking remains challenging. This is caused by the insufficient extrapolation ability of the 3D Gaussians, and by unconstrained Gaussian parameters in unobserved regions. We also believe that some of our empirical hyperparameters can be made test time adaptive e.g. our keyframe selection strategy is currently rather simplistic

Method	Metric	Rm0	Rm1	Rm2	Off0	Off1	Off2	Off3	Off4	Avg.
NICE-SLAM [84]	Depth L1 [cm]↓	1.81	1.44	2.04	1.39	1.76	8.33	4.99	2.01	2.97
	F1 [%]↑	45.0	44.8	43.6	50.0	51.9	39.2	39.9	36.5	43.9
Vox-Fusion [75]	Depth L1 [cm]↓	1.09	1.90	2.21	2.32	3.40	4.19	2.96	1.61	2.46
	F1 [%]↑	69.9	34.4	59.7	46.5	40.8	51.0	64.6	50.7	52.2
ESLAM [34]	Depth L1 [cm]↓	0.97	1.07	1.28	0.86	1.26	1.71	1.43	1.06	1.18
	F1 [%]↑	81.0	82.2	83.9	78.4	75.5	77.1	75.5	79.1	79.1
Co-SLAM [64]	Depth L1 [cm]↓	1.05	0.85	2.37	1.24	1.48	1.86	1.66	1.54	1.51
	F1 [%]↑	-	-	-	-	-	-	-	-	-
GO-SLAM [81]	Depth L1 [cm] ↓	-	-	-	-	-	-	-	-	3.38
	*Depth L1 [cm]↓	4.56	1.97	3.43	2.47	3.03	10.3	7.31	4.34	4.68
	F1 [%]↑	17.3	33.4	24.0	43.0	31.8	21.8	17.3	22.0	26.3
Point-SLAM [51]	Depth L1 [cm]↓	0.53	0.22	0.46	0.30	0.57	0.49	0.51	0.46	0.44
	F1 [%]↑	86.9	92.3	90.8	93.8	91.6	89.0	88.2	85.6	89.8
Ours	Depth L1 [cm]↓	0.69	0.33	0.83	0.52	0.46	5.43	3.74	0.47	1.56
	F1 [%]↑	88.0	90.2	88.9	92.0	90.5	83.9	81.4	86.2	87.6

Table 4. **Reconstruction Performance on Replica [57].** Our method performs on par with existing methods. *Depth L1 for GO-SLAM shows our reproduced results from random poses (GO-SLAM evaluates on ground truth poses).

Method	Rm0	Rm1	Rm2	Off0	Off1	Off2	Off3	Off4	Avg.
NICE-SLAM [84]	0.97	1.31	1.07	0.88	1.00	1.06	1.10	1.13	1.06
ESLAM [34]	0.71	0.70	0.52	0.57	0.55	0.58	0.72	0.63	0.63
Point-SLAM [51]	0.61	0.41	0.37	0.38	0.48	0.54	0.69	0.72	0.52
DROID-SLAM [63]	0.53	0.38	0.45	0.35	0.24	0.36	0.33	0.43	0.38
F2F [48]	1.64	1.92	2.8	2.48	0.8	4.55	2.64	2.27	2.38
F2GM + F2F	3.35	8.74	3.13	1.11	0.81	0.78	1.08	7.21	3.27
F2GM + F2F oracle	0.13	1.11	0.38	0.07	0.06	0.09	0.08	0.30	0.28

Table 5. **Frame-to-model tracking with 3D Gaussians on Replica [57]** (ATE-RMSE ↓ [cm]). We summarize our frame-to-Gaussian-model (F2GM) tracking experiments. We use the classical frame-to-frame tracker[48] (F2F) as the baseline. Then we evaluate the upper bound performance of the F2GM tracker which is initialized with the F2F poses and conduct refinement using pre-mapped segments obtained with ground-truth poses (F2GM + F2F oracle). This approach reaches SOTA performance on Replica novel views for tracking are never obstructed with unconstrained Gaussians. Further, we evaluate the performance of the F2GM + F2F tracker with refinement on online mapped segments. This experiment highlights the limitation of 3D Gaussians for frame-to-model tracking.
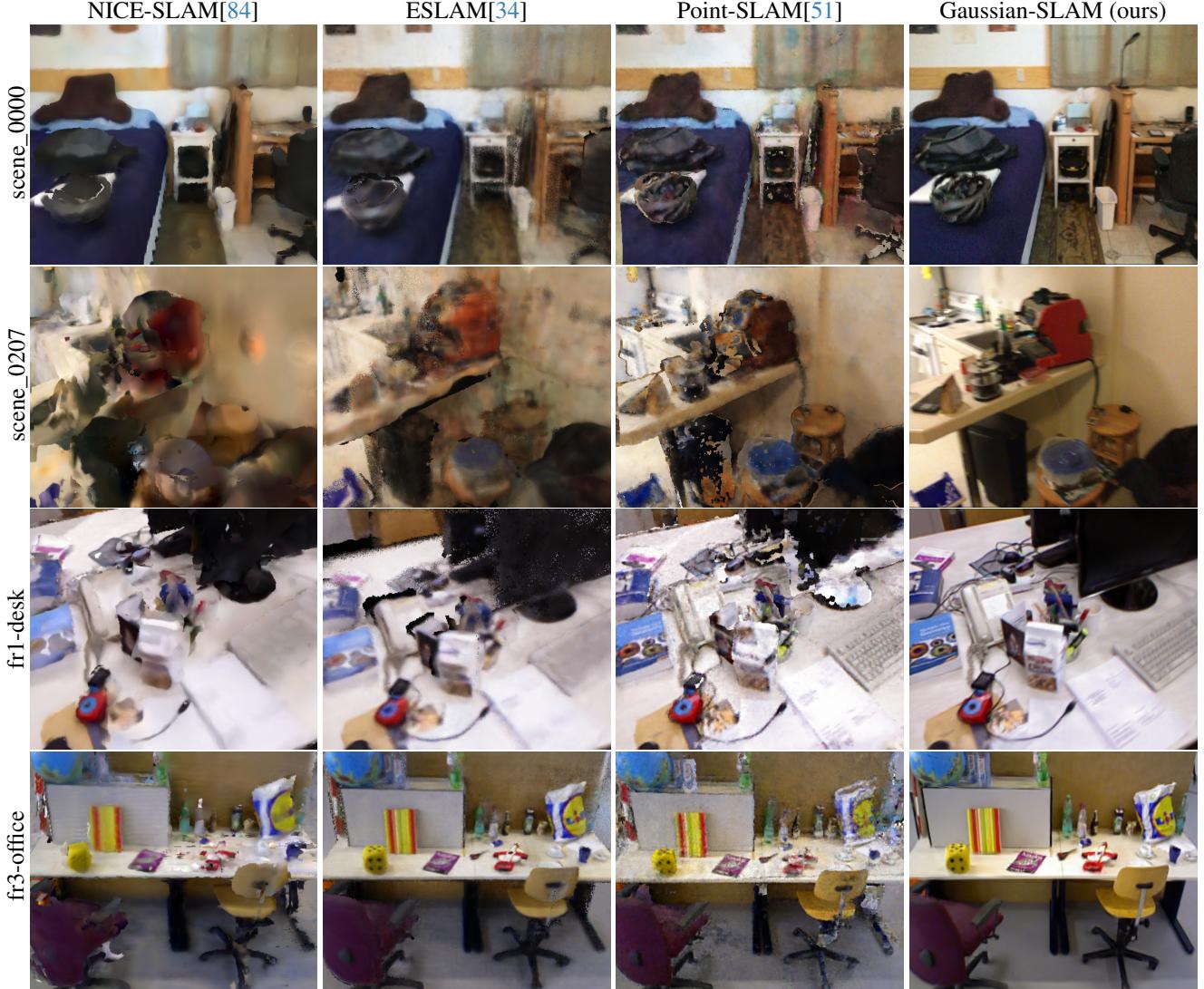
Figure 4. **Rendering performance on ScanNet [13] and TUM-RGBD [58]**. Thanks to 3D Gaussian splatting, Gaussian-SLAM is able to encode more high-frequency details and substantially increase the quality of the renderings. This is also supported by the quantitative results in Tab. 1 and Tab. 2.

Method	Mapping /Iteration	Mapping /Frame	Rendering /Frame
NICE-SLAM [84]	182 ms	10.92 s	2.64 s
Vox-Fusion [75]	55 ms	0.55 s	1.63 s
ESLAM [34]	**29 ms**	0.44 s	0.63 s
GO-SLAM [81]	-	**0.125 s**	-
Point-SLAM [51]	33 ms	2.97 s	2.96 s
Gaussian-SLAM (ours)	34 ms	1.66 s	**7.15E-07**

Table 6. **Average Mapping and Rendering Speed on Replica** `office0`. Our mapping time is competitive, while our rendering time allows for exploring mapped environments in real time. All metrics are computed using a single NVIDIA A6000.

6. Conclusion

We proposed Gaussian-SLAM, a dense SLAM system that extends and utilizes 3D Gaussian splitting for scene representation. Smart seeding and data-driven anchoring of 3D Gaussians allow us to make the optimization process efficient enough for modern neural SLAM applications. Overall, this leads to a better balance of memory and compute resource usage and the accuracy of the estimated 3D scene representation. Our experiments demonstrate that Gaussian-SLAM substantially outperforms existing solutions regarding rendering accuracy while being competitive with respect to geometry reconstruction and runtime.

A. Limitations of 3D Gaussian Splatting for SLAM

To prove the limitations discussed in Sec. 3, we conduct full-scale experiments. When naively optimizing a global Gaussian point cloud for the whole sequence we get out of memory error even for A100 NVIDIA GPUs. The cases when geometry was not encoded, or when only every single frame was optimized are shown in Tab. 7.

Method	PSNR↑	SSIM↑	LPIPS↓	F1↑	L1↓
Single-frame optimization	3.15	0.14	0.16	-	-
Color-only optimization	29.40	0.74	0.05	3	3.22
Ours	**38.90**	**0.993**	**0.069**	**87.6**	**1.56**

Table 7. The naive approach of optimizing only for a single incoming frame or only for color gives poor reconstruction and rendering results. For single-frame optimization, the geometry of the 3D Gaussians becomes so distorted that the final mesh cannot be reconstructed from the noisy depth maps rendered from it. All metrics were averaged over the 8 sequences of Replica [57] dataset.

B. Implementation Details

We use PyTorch 1.12 and Python 3.7 to implement the pipeline. Training is done with the Adam optimizer and the default hyperparameters $betas = (0.9, 0.999)$, $eps = 1e-08$ and $weight\_decay = 0$. The results are gathered using NVIDIA A6000 and A100 GPUs. Different learning rates are used for different Gaussian parameters. γ is set to 0.0025 for the first 3 channels of features of spherical harmonics and is 20 times smaller for the rest of the features. Learning rates of 0.05, 0.005, and 0.001 are set for opacity, scaling, and rotation parameters. During training, we set the spherical harmonics degree to 0 since we assume that the colors are not view-dependent within every sub-map.

C. Evaluation Metrics

Mapping. We use the following five metrics to quantify the reconstruction performance. We compare the ground truth mesh to the predicted mesh. The F-score is defined as the harmonic mean between Precision (P) and Recall (R), $F = 2\frac{PR}{P+R}$. Precision is defined as the percentage of points on the predicted mesh that lie within some distance τ from a point on the ground truth mesh. Vice versa, Recall is defined as the percentage of points on the ground truth mesh that lies within the same distance τ from a point on the predicted mesh. In all our experiments, we use the distance threshold $\tau = 0.01$ m. Before the Precision and Recall are computed, the input meshes are globally aligned with the iterative closest point (ICP) algorithm. We use the evaluation script provided by the authors of [51][1]. Finally, we report the

[1] https://github.com/tfy14esa/evaluate_3d_reconstruction_lib

depth L1 metric which renders depth maps from randomly sampled viewpoints from the reconstructed and ground truth meshes. The depth maps are then compared and the L1 error is reported and averaged over 1000 sampled views. We use the evaluation code provided by [84].

Tracking. We use the absolute trajectory error (ATE) RMSE [59] to compare tracking error across methods. This computes the translation difference between the estimated trajectory and the ground truth. Before evaluating the ATE RMSE, we align the trajectories with Horn's closed-form solution [18].

D. Additional Experiments

Influence of the Number of Iterations. The number of iterations spent per frame is one of the most important parameters of our method. It directly influences both runtime and rendering. In 5 we show that while our method achieves best results with a larger amount of iterations, it is still state of the art in rendering with fewer iterations.
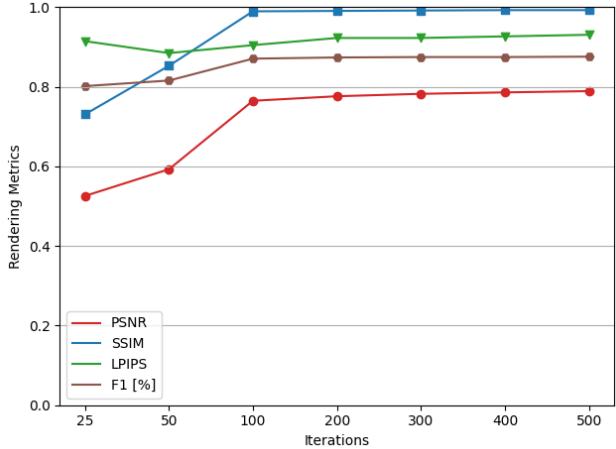

Figure 5. **Ablation over different of iterations spent per frame on the Replica[57] dataset.** The iteration number is a hyperparameter allowing for finding a balance between speed and rendering and reconstruction quality. A smaller number of iterations dramatically reduces the runtime, while sacrificing only a bit of rendering performance. *PSNR* is divided by 50 to be in [0, 1] range, *LPIPS* in the diagram is the inverse of the original LPIPS.

Influence of the sub-map Size. Another important parameter is the sub-map size. It influences the runtime and the rendering and reconstruction quality. The sub-map size does not correlate much with the rendering metrics but can improve the runtime since more iterations are spent on the first frames of the new sub-map. This holds for both synthetic and real-world datasets as shown in 7 and 6.

Additional Tracking Experiments. Tab. 8 provides additional results comparing tracking performance on TUM-RGBD [58] for frame-to-frame tracker (F2F), frame-to-
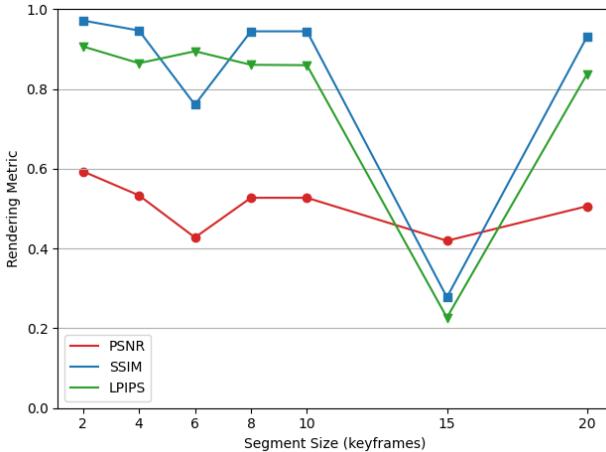
Figure 6. Ablation over different sizes of the map segments on TUM-RGBD[58] dataset. Segment size is a hyperparameter allowing for finding a balance between speed and rendering quality. *PSNR* is divided by 50 to be in [0, 1] range, *LPIPS* in the diagram is the inverse of the original LPIPS, *Depth L1* is on the log scale.
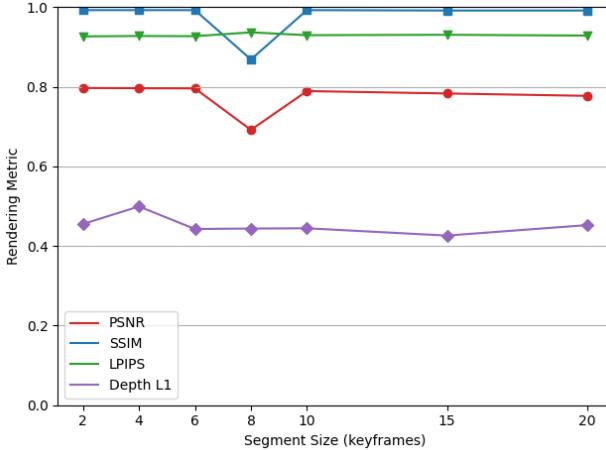

Figure 7. Ablation over different sizes of the map segments on Replica[57] dataset. Segment size is a hyperparameter allowing for finding a balance between speed and rendering and reconstruction quality. *PSNR* is divided by 50, *LPIPS* in the diagram is the inverse of the original LPIPS, *Depth L1* is on the log scale.

Method	fr1/ desk	fr1/ desk2	fr1/ room	fr2/ xyz	fr3/ office	Avg.
BAD-SLAM [53]	1.7	N/A	N/A	1.1	1.7	N/A
Kintinuous [70]	3.7	7.1	7.5	2.9	3.0	4.84
ORB-SLAM2 [40]	1.6	2.2	4.7	0.4	1.0	1.98
ElasticFusion [71]	2.53	6.83	21.49	1.17	2.52	6.91
DROID-SLAM [63]	1.80	2.11	3.13	0.33	1.32	1.74
NICE-SLAM [84]	4.26	4.99	34.49	31.73 (6.19)	3.87	15.87 (10.76)
Vox-Fusion* [75]	3.52	6.00	19.53	1.49	26.01	11.31
Point-SLAM [51]	4.34	4.54	30.92	1.31	3.48	8.92
F2F	3.25	6.56	28.49	5.34	25.15	13.76
F2GM + F2F	14.43	24.55	44.83	2.75	6.71	18.66
F2GM + F2F oracle	3.04	10.85	3.03	0.28	1.07	3.65

Table 8. **Frame-to-model Tracking with 3D Gaussians on TUM-RGBD [59]** (ATE RMSE ↓ [cm]). Currently the frame-to-Gaussian-model tracking in Gaussian-SLAM yields large drift, while the oracle performance shows great potential. In parenthesis the average over only the successful runs is reported. Part of the numbers are taken from [51].

in real-world reconstructions.

Gaussian-model tracker which is initialized with the F2F poses following by refinement using online mapped segments (F2GM+F2F), and lastly the F2GM tracker which is initialized with the F2F poses and conduct refinement using pre-mapped segments obtained with ground-truth poses (F2GM+F2F oracle).

Qualitative Reconstruction Results. Fig. 8 shows reconstructed mesh on Replica dataset with a normal map shader to highlight the difference. Fig. 9 compares colored mesh on ScanNet [13] and TUM-RGBD [58] scenes. Gaussian-SLAM is able to recover more geometric and color details
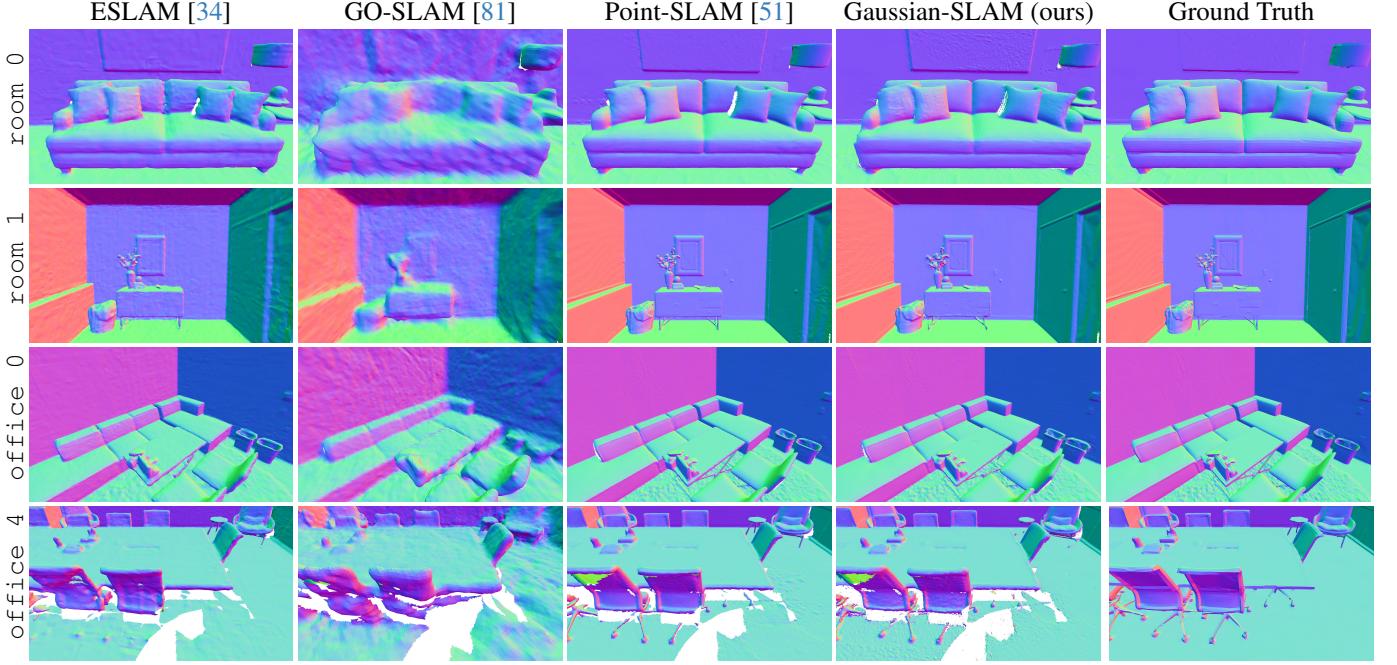
Figure 8. **Qualitative Reconstruction Comparison on the Replica dataset [57]**. Gaussian-SLAM achieves comparable reconstruction performance with the state-of-the-art dense neural SLAM methods.
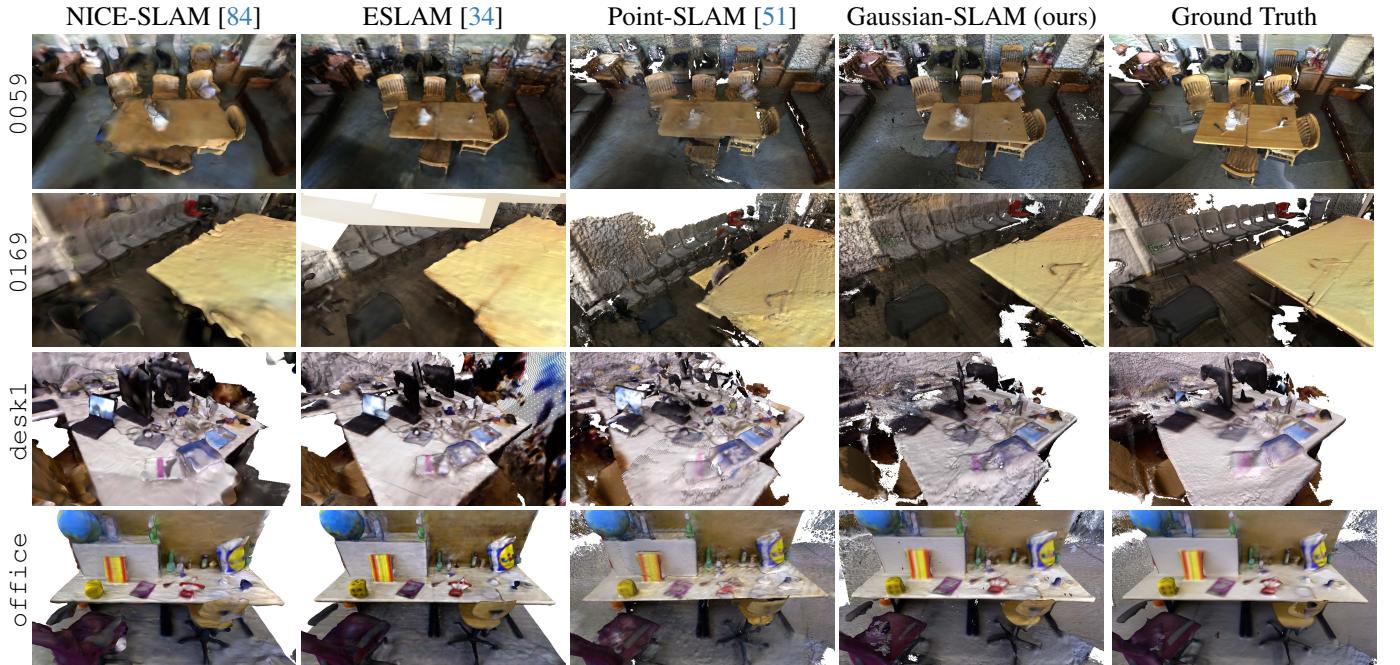

Figure 9. **Qualitative Mesh-based Comparison on ScanNet[13] and TUM-RGBD[58] datasets.** For TUM-RGBD, the ground truth is obtained by TSDF fusion. NICE-SLAM[84] shows over-smoothed surfaces. Point-SLAM[51] has duplicated geometry. ESLAM[34] improves the reconstruction quality, while Gaussian-SLAM is moderately better in recovering geometric details, see the chairs in scene_0059 for example.

References

[1] Dejan Azinović, Ricardo Martin-Brualla, Dan B Goldman, Matthias Nießner, and Justus Thies. Neural rgb-d surface reconstruction. In *IEEE/CVF Conference on Computer Vision and Pattern Recognition*, pages 6290–6301, 2022. 2

[2] Marcelo Bertalmio, Andrea L Bertozzi, and Guillermo Sapiro. Navier-stokes, fluid dynamics, and image and video inpainting. In *Proceedings of the 2001 IEEE Computer Society Conference on Computer Vision and Pattern Recognition. CVPR 2001*, pages I–355. IEEE, 2001. 5

[3] Wenjing Bian, Zirui Wang, Kejie Li, Jia-Wang Bian, and Victor Adrian Prisacariu. Nope-nerf: Optimising neural radiance field with no pose prior. *arXiv preprint arXiv:2212.07388*, 2022. 2

[4] Aljaž Božič, Pablo Palafox, Justus Thies, Angela Dai, and Matthias Nießner. Transformerfusion: Monocular rgb scene reconstruction using transformers. *arXiv preprint arXiv:2107.02191*, 2021. 2

[5] E. Bylow, C. Olsson, and F. Kahl. Robust online 3d reconstruction combining a depth sensor and sparse feature points. *Unknown Journal*, Unknown Volume(Unknown Number): Unknown Pages, Unknown Year. 2

[6] Yan-Pei Cao, Leif Kobbelt, and Shi-Min Hu. Real-time high-accuracy three-dimensional reconstruction with consumer rgb-d cameras. *ACM Transactions on Graphics (TOG)*, 37(5): 1–16, 2018. 2

[7] Jiawen Chen, Dennis Bautembach, and Shahram Izadi. Scalable real-time volumetric surface reconstruction. *ACM Transactions on Graphics (ToG)*, 32(4):1–16, 2013. 2

[8] Hae Min Cho, HyungGi Jo, and Euntai Kim. Sp-slam: Surfel-point simultaneous localization and mapping. *IEEE/ASME Transactions on Mechatronics*, 27(5):2568–2579, 2021. 2

[9] Jaesung Choe, Sunghoon Im, Francois Rameau, Minjun Kang, and In So Kweon. Volumefusion: Deep depth fusion for 3d scene reconstruction. In *IEEE/CVF International Conference on Computer Vision (ICCV)*, pages 16086–16095, 2021. 2

[10] Sungjoon Choi, Qian-Yi Zhou, and Vladlen Koltun. Robust reconstruction of indoor scenes. In *Proceedings of the IEEE conference on computer vision and pattern recognition*, pages 5556–5565, 2015. 2

[11] Chi-Ming Chung, Yang-Che Tseng, Ya-Ching Hsu, Xiang-Qian Shi, Yun-Hung Hua, Jia-Fong Yeh, Wen-Chin Chen, Yi-Ting Chen, and Winston H Hsu. Orbeez-slam: A real-time monocular visual slam with orb features and nerf-realized mapping. *arXiv preprint arXiv:2209.13274*, 2022. 2

[12] Brian Curless and Marc Levoy. Volumetric method for building complex models from range images. In *SIGGRAPH Conference on Computer Graphics*. ACM, 1996. 2, 6

[13] Angela Dai, Angel X. Chang, Manolis Savva, Maciej Halber, Thomas Funkhouser, and Matthias Nießner. ScanNet: Richly-annotated 3D reconstructions of indoor scenes. In *Conference on Computer Vision and Pattern Recognition (CVPR)*. IEEE/CVF, 2017. 6, 7, 8, 10, 11

[14] Angela Dai, Matthias Nießner, Michael Zollhöfer, Shahram Izadi, and Christian Theobalt. Bundlefusion: Real-time globally consistent 3d reconstruction using on-the-fly surface reintegration. *ACM Transactions on Graphics (ToG)*, 36(4):1, 2017. 1, 2, 7

[15] Andrew J Davison, Ian D Reid, Nicholas D Molton, and Olivier Stasse. Monoslam: Real-time single camera slam. *IEEE transactions on pattern analysis and machine intelligence*, 29(6):1052–1067, 2007. 1

[16] Jorge Fuentes-Pacheco, José Ruiz-Ascencio, and Juan Manuel Rendón-Mancha. Visual simultaneous localization and mapping: a survey. *Artificial intelligence review*, 43:55–81, 2015. 1

[17] Yiming Gao, Yan-Pei Cao, and Ying Shan. Surfelnerf: Neural surfel radiance fields for online photorealistic reconstruction of indoor scenes. In *Proceedings of the IEEE/CVF Conference on Computer Vision and Pattern Recognition*, pages 108–118, 2023. 3

[18] Berthold KP Horn. Closed-form solution of absolute orientation using unit quaternions. *Josa a*, 4(4):629–642, 1987. 9

[19] Jiahui Huang, Shi-Sheng Huang, Haoxuan Song, and Shi-Min Hu. Di-fusion: Online implicit 3d reconstruction with deep priors. In *IEEE/CVF Conference on Computer Vision and Pattern Recognition*, pages 8932–8941, 2021. 1, 2

[20] Jeff Johnson, Matthijs Douze, and Hervé Jégou. Billion-scale similarity search with GPUs. *IEEE Transactions on Big Data*, 7(3):535–547, 2019. 6

[21] Olaf Kähler, Victor Prisacariu, Julien Valentin, and David Murray. Hierarchical voxel block hashing for efficient integration of depth images. *IEEE Robotics and Automation Letters*, 1(1):192–197, 2015. 2

[22] Olaf Kähler, Victor Adrian Prisacariu, Carl Yuheng Ren, Xin Sun, Philip H. S. Torr, and David William Murray. Very high frame rate volumetric integration of depth images on mobile devices. *IEEE Trans. Vis. Comput. Graph.*, 21(11): 1241–1250, 2015. 2

[23] Iman Abaspur Kazerouni, Luke Fitzgerald, Gerard Dooly, and Daniel Toal. A survey of state-of-the-art on visual slam. *Expert Systems with Applications*, 205:117734, 2022. 1

[24] Maik Keller, Damien Lefloch, Martin Lambers, Shahram Izadi, Tim Weyrich, and Andreas Kolb. Real-time 3d reconstruction in dynamic scenes using point-based fusion. In *International Conference on 3D Vision (3DV)*, pages 1–8. IEEE, 2013. 2

[25] Bernhard Kerbl, Georgios Kopanas, Thomas Leimkühler, and George Drettakis. 3d gaussian splatting for real-time radiance field rendering. *ACM Transactions on Graphics*, 42(4), 2023. 1, 3, 4, 5

[26] Georg Klein and David Murray. Parallel tracking and mapping for small ar workspaces. In *2007 6th IEEE and ACM international symposium on mixed and augmented reality*, pages 225–234. IEEE, 2007. 1

[27] Heng Li, Xiaodong Gu, Weihao Yuan, Luwei Yang, Zilong Dong, and Ping Tan. Dense rgb slam with neural implicit maps. *arXiv preprint arXiv:2301.08930*, 2023. 2

[28] Kejie Li, Yansong Tang, Victor Adrian Prisacariu, and Philip HS Torr. Bnv-fusion: Dense 3d reconstruction using bi-level neural volume fusion. In *IEEE/CVF Conference on Computer Vision and Pattern Recognition*, pages 6166–6175, 2022. 2

[29] Chen Hsuan Lin, Wei Chiu Ma, Antonio Torralba, and Simon Lucey. BARF: Bundle-Adjusting Neural Radiance Fields. In *International Conference on Computer Vision (ICCV)*. IEEE/CVF, 2021. 2

[30] Dongrui Liu, Chuanchaun Chen, Changqing Xu, Robert C Qiu, and Lei Chu. Self-supervised point cloud registration with deep versatile descriptors for intelligent driving. *IEEE Transactions on Intelligent Transportation Systems*, 2023. 2

[31] Lingjie Liu, Jiatao Gu, Kyaw Zaw Lin, Tat-Seng Chua, and Christian Theobalt. Neural sparse voxel fields. In *Advances in Neural Information Processing Systems*, pages 15651–15663, 2020. 2

[32] William E Lorensen and Harvey E Cline. Marching cubes: A high resolution 3d surface construction algorithm. *ACM siggraph computer graphics*, 21(4):163–169, 1987. 7

[33] Jonathon Luiten, Georgios Kopanas, Bastian Leibe, and Deva Ramanan. Dynamic 3d gaussians: Tracking by persistent dynamic view synthesis, 2023. 3

[34] Mohammad Mahdi Johari, Camilla Carta, and François Fleuret. Eslam: Efficient dense slam system based on hybrid representation of signed distance fields. *arXiv e-prints*, pages arXiv–2211, 2022. 1, 2, 3, 6, 7, 8, 11

[35] Nico Marniok, Ole Johannsen, and Bastian Goldluecke. An efficient octree design for local variational range image fusion. In *German Conference on Pattern Recognition (GCPR)*, pages 401–412. Springer, 2017. 2

[36] Lars Mescheder, Michael Oechsle, Michael Niemeyer, Sebastian Nowozin, and Andreas Geiger. Occupancy networks: Learning 3d reconstruction in function space. In *IEEE/CVF conference on computer vision and pattern recognition*, pages 4460–4470, 2019. 2

[37] Marko Mihajlovic, Silvan Weder, Marc Pollefeys, and Martin R Oswald. Deepsurfels: Learning online appearance fusion. In *IEEE/CVF Conference on Computer Vision and Pattern Recognition*, pages 14524–14535, 2021. 3

[38] Ben Mildenhall, Pratul P. Srinivasan, Matthew Tancik, Jonathan T. Barron, Ravi Ramamoorthi, and Ren Ng. NeRF: Representing Scenes as Neural Radiance Fields for View Synthesis. In *European Conference on Computer Vision (ECCV)*. CVF, 2020. 1, 2

[39] Thomas Müller, Alex Evans, Christoph Schied, and Alexander Keller. Instant neural graphics primitives with a multiresolution hash encoding. *ACM Transactions on Graphics (ToG)*, 41(4):1–15, 2022. 2

[40] Raul Mur-Artal and Juan D. Tardos. ORB-SLAM2: An Open-Source SLAM System for Monocular, Stereo, and RGB-D Cameras. *IEEE Transactions on Robotics*, 33(5):1255–1262, 2017. 1, 10

[41] Zak Murez, Tarrence van As, James Bartolozzi, Ayan Sinha, Vijay Badrinarayanan, and Andrew Rabinovich. Atlas: End-to-end 3d scene reconstruction from posed images. In *Computer Vision–ECCV 2020: 16th European Conference, Glasgow, UK, August 23–28, 2020, Proceedings, Part VII 16*, pages 414–431. Springer, 2020. 2

[42] Richard A Newcombe, Shahram Izadi, Otmar Hilliges, David Molyneaux, David Kim, Andrew J Davison, Pushmeet Kohli, Jamie Shotton, Steve Hodges, and Andrew W Fitzgibbon. Kinectfusion: Real-time dense surface mapping and tracking. In *ISMAR*, pages 127–136, 2011. 1, 2

[43] Richard A Newcombe, Steven J Lovegrove, and Andrew J Davison. Dtam: Dense tracking and mapping in real-time. In *International Conference on Computer Vision (ICCV)*, 2011. 1, 2

[44] Matthias Nießner, Michael Zollhöfer, Shahram Izadi, and Marc Stamminger. Real-time 3d reconstruction at scale using voxel hashing. *ACM Transactions on Graphics (TOG)*, 32, 2013. 1, 2

[45] Michael Oechsle, Songyou Peng, and Andreas Geiger. UNISURF: Unifying Neural Implicit Surfaces and Radiance Fields for Multi-View Reconstruction. In *International Conference on Computer Vision (ICCV)*. IEEE/CVF, 2021. 2

[46] Helen Oleynikova, Zachary Taylor, Marius Fehr, Roland Siegwart, and Juan I. Nieto. Voxblox: Incremental 3d euclidean signed distance fields for on-board MAV planning. In *2017 IEEE/RSJ International Conference on Intelligent Robots and Systems, IROS 2017, Vancouver, BC, Canada, September 24-28, 2017*, pages 1366–1373. IEEE, 2017. 2

[47] Joseph Ortiz, Alexander Clegg, Jing Dong, Edgar Sucar, David Novotny, Michael Zollhoefer, and Mustafa Mukadam. isdf: Real-time neural signed distance fields for robot perception. *arXiv preprint arXiv:2204.02296*, 2022. 2

[48] Jaesik Park, Qian-Yi Zhou, and Vladlen Koltun. Colored point cloud registration revisited. In *Proceedings of the IEEE international conference on computer vision*, pages 143–152, 2017. 5, 7

[49] Songyou Peng, Michael Niemeyer, Lars Mescheder, Marc Pollefeys, and Andreas Geiger. Convolutional Occupancy Networks. In *European Conference Computer Vision (ECCV)*. CVF, 2020. 3

[50] Antoni Rosinol, John J. Leonard, and Luca Carlone. NeRF-SLAM: Real-Time Dense Monocular SLAM with Neural Radiance Fields. *arXiv*, 2022. 2

[51] Erik Sandström, Yue Li, Luc Van Gool, and Martin R Oswald. Point-slam: Dense neural point cloud-based slam. In *International Conference on Computer Vision (ICCV)*. IEEE/CVF, 2023. 1, 2, 4, 6, 7, 8, 9, 10, 11

[52] Mohamed Sayed, John Gibson, Jamie Watson, Victor Prisacariu, Michael Firman, and Clément Godard. Simplerecon: 3d reconstruction without 3d convolutions. In *European Conference on Computer Vision*, pages 1–19. Springer, 2022. 2

[53] Thomas Schops, Torsten Sattler, and Marc Pollefeys. BAD SLAM: Bundle adjusted direct RGB-D SLAM. In *CVF/IEEE Conference on Computer Vision and Pattern Recognition (CVPR)*, 2019. 1, 2, 10

[54] Frank Steinbrücker, Jürgen Sturm, and Daniel Cremers. Real-time visual odometry from dense rgb-d images. In *2011 IEEE international conference on computer vision workshops (ICCV Workshops)*, pages 719–722. IEEE, 2011. 7

[55] Frank Steinbrucker, Christian Kerl, and Daniel Cremers. Large-scale multi-resolution surface reconstruction from rgb-d sequences. In *IEEE International Conference on Computer Vision*, pages 3264–3271, 2013. 2

[56] Noah Stier, Alexander Rich, Pradeep Sen, and Tobias Höllerer. Vortx: Volumetric 3d reconstruction with transformers for

voxelwise view selection and fusion. In *2021 International Conference on 3D Vision (3DV)*, pages 320–330. IEEE, 2021. 2

[57] Julian Straub, Thomas Whelan, Lingni Ma, Yufan Chen, Erik Wijmans, Simon Green, Jakob J Engel, Raul Mur-Artal, Carl Ren, Shobhit Verma, et al. The replica dataset: A digital replica of indoor spaces. *arXiv preprint arXiv:1906.05797*, 2019. 6, 7, 9, 10, 11

[58] Jan Stühmer, Stefan Gumhold, and Daniel Cremers. Real-time dense geometry from a handheld camera. In *Joint Pattern Recognition Symposium*, pages 11–20. Springer, 2010. 1, 6, 8, 9, 10, 11

[59] Jürgen Sturm, Nikolas Engelhard, Felix Endres, Wolfram Burgard, and Daniel Cremers. A benchmark for the evaluation of RGB-D SLAM systems. In *International Conference on Intelligent Robots and Systems (IROS)*. IEEE/RSJ, 2012. 1, 6, 7, 9, 10

[60] Edgar Sucar, Shikun Liu, Joseph Ortiz, and Andrew J. Davison. iMAP: Implicit Mapping and Positioning in Real-Time. In *International Conference on Computer Vision (ICCV)*. IEEE/CVF, 2021. 1, 2, 7

[61] Jiaming Sun, Yiming Xie, Linghao Chen, Xiaowei Zhou, and Hujun Bao. Neuralrecon: Real-time coherent 3d reconstruction from monocular video. In *IEEE/CVF Conference on Computer Vision and Pattern Recognition*, pages 15598–15607, 2021. 2

[62] Yijie Tang, Jiazhao Zhang, Zhinan Yu, He Wang, and Kai Xu. Mips-fusion: Multi-implicit-submaps for scalable and robust online neural rgb-d reconstruction. *arXiv preprint arXiv:2308.08741*, 2023. 1

[63] Zachary Teed and Jia Deng. Droid-slam: Deep visual slam for monocular, stereo, and rgb-d cameras. *Advances in neural information processing systems*, 34:16558–16569, 2021. 6, 7, 10

[64] Hengyi Wang, Jingwen Wang, and Lourdes Agapito. Co-slam: Joint coordinate and sparse parametric encodings for neural real-time slam. In *Proceedings of the IEEE/CVF Conference on Computer Vision and Pattern Recognition*, pages 13293–13302, 2023. 1, 2, 7

[65] Jiepeng Wang, Peng Wang, Xiaoxiao Long, Christian Theobalt, Taku Komura, Lingjie Liu, and Wenping Wang. Neuris: Neural reconstruction of indoor scenes using normal priors. In *Computer Vision–ECCV 2022: 17th European Conference, Tel Aviv, Israel, October 23–27, 2022, Proceedings, Part XXXII*, pages 139–155. Springer, 2022. 2

[66] Zhou Wang, Alan C Bovik, Hamid R Sheikh, and Eero P Simoncelli. Image quality assessment: from error visibility to structural similarity. *IEEE transactions on image processing*, 13(4):600–612, 2004. 5, 7

[67] Zirui Wang, Shangzhe Wu, Weidi Xie, Min Chen, and Victor Adrian Prisacariu. Nerf--: Neural radiance fields without known camera parameters. *arXiv preprint arXiv:2102.07064*, 2021. 2

[68] Silvan Weder, Johannes Schonberger, Marc Pollefeys, and Martin R Oswald. Routedfusion: Learning real-time depth map fusion. In *IEEE/CVF Conference on Computer Vision and Pattern Recognition*, pages 4887–4897, 2020. 2

[69] Silvan Weder, Johannes L Schonberger, Marc Pollefeys, and Martin R Oswald. Neuralfusion: Online depth fusion in latent space. In *IEEE/CVF Conference on Computer Vision and Pattern Recognition*, pages 3162–3172, 2021. 2

[70] Thomas Whelan, John McDonald, Michael Kaess, Maurice Fallon, Hordur Johannsson, and John J. Leonard. Kintinuous: Spatially extended kinectfusion. In *Proceedings of RSS '12 Workshop on RGB-D: Advanced Reasoning with Depth Cameras*, 2012. 10

[71] Thomas Whelan, Stefan Leutenegger, Renato Salas-Moreno, Ben Glocker, and Andrew Davison. Elasticfusion: Dense slam without a pose graph. In *Robotics: Science and Systems (RSS)*, 2015. 1, 2, 10

[72] Guanjun Wu, Taoran Yi, Jiemin Fang, Lingxi Xie, Xiaopeng Zhang, Wei Wei, Wenyu Liu, Qi Tian, and Xinggang Wang. 4d gaussian splatting for real-time dynamic scene rendering, 2023. 3

[73] Qiangeng Xu, Zexiang Xu, Julien Philip, Sai Bi, Zhixin Shu, Kalyan Sunkavalli, and Ulrich Neumann. Point-nerf: Point-based neural radiance fields. In *IEEE/CVF Conference on Computer Vision and Pattern Recognition*, pages 5438–5448, 2022. 2

[74] Zike Yan, Yuxin Tian, Xuesong Shi, Ping Guo, Peng Wang, and Hongbin Zha. Continual neural mapping: Learning an implicit scene representation from sequential observations. In *IEEE/CVF International Conference on Computer Vision (ICCV)*, pages 15782–15792, 2021. 2

[75] Xingrui Yang, Hai Li, Hongjia Zhai, Yuhang Ming, Yuqian Liu, and Guofeng Zhang. Vox-fusion: Dense tracking and mapping with voxel-based neural implicit representation. In *IEEE International Symposium on Mixed and Augmented Reality (ISMAR)*, pages 499–507. IEEE, 2022. 2, 6, 7, 8, 10

[76] Xingrui Yang, Yuhang Ming, Zhaopeng Cui, and Andrew Calway. Fd-slam: 3-d reconstruction using features and dense matching. In *2022 International Conference on Robotics and Automation (ICRA)*, pages 8040–8046. IEEE, 2022. 2

[77] Ziyi Yang, Xinyu Gao, Wen Zhou, Shaohui Jiao, Yuqing Zhang, and Xiaogang Jin. Deformable 3d gaussians for high-fidelity monocular dynamic scene reconstruction, 2023. 3

[78] Zeyu Yang, Hongye Yang, Zijie Pan, Xiatian Zhu, and Li Zhang. Real-time photorealistic dynamic scene representation and rendering with 4d gaussian splatting, 2023. 3

[79] Heng Zhang, Guodong Chen, Zheng Wang, Zhenhua Wang, and Lining Sun. Dense 3d mapping for indoor environment based on feature-point slam method. In *2020 the 4th International Conference on Innovation in Artificial Intelligence*, pages 42–46, 2020. 2

[80] Richard Zhang, Phillip Isola, Alexei A Efros, Eli Shechtman, and Oliver Wang. The unreasonable effectiveness of deep features as a perceptual metric. In *IEEE conference on computer vision and pattern recognition*, pages 586–595, 2018. 7

[81] Youmin Zhang, Fabio Tosi, Stefano Mattoccia, and Matteo Poggi. Go-slam: Global optimization for consistent 3d instant reconstruction. *arXiv preprint arXiv:2309.02436*, 2023. 1, 2, 7, 8, 11

[82] Qian-Yi Zhou and Vladlen Koltun. Dense scene reconstruction with points of interest. *ACM Transactions on Graphics (TOG)*, 32(4):120, 2013. 2

[83] Qian-Yi Zhou, Stephen Miller, and Vladlen Koltun. Elastic fragments for dense scene reconstruction. *Proceedings of the IEEE International Conference on Computer Vision*, pages 2726–2733, 2013.

[84] Zihan Zhu, Songyou Peng, Viktor Larsson, Weiwei Xu, Hujun Bao, Zhaopeng Cui, Martin R Oswald, and Marc Pollefeys. Nice-slam: Neural implicit scalable encoding for slam. In *IEEE/CVF Conference on Computer Vision and Pattern Recognition*, pages 12786–12796, 2022. 1, 2, 6, 7, 8, 9, 10, 11

[85] Zihan Zhu, Songyou Peng, Viktor Larsson, Zhaopeng Cui, Martin R Oswald, Andreas Geiger, and Marc Pollefeys. Nicer-slam: Neural implicit scene encoding for rgb slam. *arXiv preprint arXiv:2302.03594*, 2023. 2, 6

[86] Michael Zollhöfer, Patrick Stotko, Andreas Görlitz, Christian Theobalt, Matthias Nießner, Reinhard Klein, and Andreas Kolb. State of the art on 3d reconstruction with rgb-d cameras. In *Computer graphics forum*, pages 625–652. Wiley Online Library, 2018. 2

[87] Matthias Zwicker, Hanspeter Pfister, Jeroen Van Baar, and Markus Gross. Surface splatting. In *Proceedings of the 28th annual conference on Computer graphics and interactive techniques*, pages 371–378, 2001. 3